Plasma Chemistry and Plasma Processing
https://doi.org/10.1007/s11090-023-10374-3

ORIGINAL PAPER

Impact of Residual Surface Charges on Energy Coupling of Packed-Bed Dielectric Barrier Discharge: A Simulation Investigation

Chenhua Ren[1,3] · Bangdou Huang[1] · Yi Luo[1] · Cheng Zhang[1,2] · Tao Shao[1,2]

Received: 15 May 2023 / Accepted: 5 August 2023

Abstract
Packed-bed dielectric barrier discharge (PB DBD) is a promising reactor for plasma catalysis, while the charge accumulation on the dielectric surface significantly affects the discharge dynamics and plasma chemistry. In this work, the role of residual surface charges in PB DBD reactor driven by repetitively high-voltage (HV) pulse with different polarities and pulse sequences is investigated, based on a two-dimensional fluid model. For the positive pulse, both charge transfer and energy deposition are elevated with negative HV as the previous pulse (i.e. bipolar mode), while they are suppressed with unipolar pulses. However, for negative polarity, the intense charge accumulation greatly enhances energy deposition regardless of operating modes, which is due to that a sufficient field enhancement caused by residual surface charges can directly lead to the breakdown between the packing beads gap, and thus promotes the discharge. The presence of residual surface charges alters the electric field distribution at the streamer front and plasma channel, regulates the percentage of power density deposited in these regions, and further dictates the energy branching into different processes. The results in this work illustrate the regulation effect of residual charges on the energy coupling of the PB DBD, which is beneficial to specifically improve the plasma-catalysis performance.

Keywords Dielectric barrier discharge · Packed bed · Plasma catalysis · Residual surface charge

✉ Bangdou Huang
huangbangdou@mail.iee.ac.cn

✉ Tao Shao
st@mail.iee.ac.cn

[1] Beijing International S&T Cooperation Base for Plasma Science and Energy Conversion, Institute of Electrical Engineering, Chinese Academy of Sciences, Beijing 100190, China

[2] University of Chinese Academy of Sciences, Beijing 100049, China

[3] North China Electric Power University, Beijing 102206, China

Published online: 22 August 2023

Introduction

Plasma-catalysis, based on the integration of non-equilibrium plasma and heterogeneous catalysts, is a promising approach to regulate the energy efficiency and catalytic activity of the chemical process [1, 2]. Packed-bed dielectric barrier discharge (PB DBD) at atmospheric pressure, combing the local field enhancement between packing materials and the better product selectivity [3, 4], has attracted extensive interest in various environmental applications, such as CO_2 conversion [5–7], nitrogen fixation [8–10], and ozone generation [11, 12].

The filled dielectric pellets/beads in PB DBD reactors can provide a sufficient contact between the plasma and the catalysts, resulting in an improved synergistic effect [13–15]. For example, the introduction of packing dielectrics (e.g. Al_2O_3) leads to an increment in the power density due to the intense micro-discharges, which greatly enhances the energy efficiency for decomposition of CO_2 [16–19]. Nevertheless, plasma-catalysis is essentially a multi-parameter process with a high degree of coupling between the discharge, chemical, and thermodynamic effects [20, 21].

Such a high specific surface area inevitably amplifies the impact of charges on the discharge properties [22, 23], which affects the morphology and dynamics of volume/surface streamers by distorting the electric field distribution, thereby altering the energy coupling and branching [24–26]. Furthermore, since the relaxation time of surface charges can last up to several hours (depending on the dielectric conductivity), the accumulation effect of residual surface charges is believed to play a critical role on subsequent discharges, especially under repetitive pulses [27, 28].

In experiments, there are several approaches to trace surface charge or reveal its cumulative effect on the discharges, e.g. by adopting electro-optical crystals based on the Pockels-effect or using the non-intrusive electric field induced second harmonic (EFISH) method [29–32]. However, the application of optical diagnostics is restricted to the PB DBD reactors, due to the invisibility caused by the block of beads and its complex spatial layout [33].

Recently, numerous computational studies have been conducted to investigate the effect of packing material properties (size, shape, and dielectric constant) [34–36], various beads arrangements [37–40], and topology of metallic catalysts [41, 42] on the plasma-surface interactions, based on the particle-in-cell/Monte Carlo collision model or the fluid model. Even though the importance of surface changing on the electric field enhancement and the streamer propagation during a single discharge have been revealed, the accumulation effect of surface charges on the characteristics of subsequent discharges, e.g. discharge dynamics and energy deposition, is still lacking.

In this work, the impact of residual surface charge on the properties of PB DBD, and its contribution to the energy coupling and branching are investigated by using a two-dimensional fluid model. The spatial distribution and the branching pathway of deposited energy are illustrated. Dynamics of instantaneous power density, energy branching, and electric field in various discharge operating modes for both polarities are demonstrated.

Model Description

The fluid modeling of PB DBD is conducted based on the 2D PASSKEy (PArallel Streamer Solver with KinEtics) framework [43]. Detailed numerical methods and validation can be found in [44, 45]. The equations solved and implementation of fluid model are briefly presented in Appendix.

Treatment of Residual Surface Charges

To consider the impact of residual surface charges on the properties of subsequent discharge, a simplified treatment has been proposed and implemented in our previous work [46]. Three characteristic times are considered, namely the recombination time τ_r between space charges (positive and negative ions), the diffusion time τ_d of ions in the gas phase to the dielectric surface, and the relaxation time of surface charges τ_s, respectively. As demonstrated in [46], the relationship $\tau_s >> \tau_d >> \tau_r$ are satisfied, which means that the decay of surface charges and its neutralization caused by space ions can be ignored during the pulse interval (typically on the order of μs to ms [27, 28]).

Thus, in this work, two discharges under positive and negative polarity without prepulse are first calculated (single mode). The preserved surface charges are then used as the initial boundary for the subsequent pulse, and discharge operates in the bipolar and unipolar modes, depending on the polarity between the previous and current pulse.

Geometry and Conditions

The 2D cartesian computational domain of the coaxial PB DBD structure 5×5 mm is shown in Fig. 1. The HV electrode (red region) with radius of 100 μm and the ground electrode located on the periphery are separated by two dielectric layers. For both sides, the total thickness of dielectric layer and electrode is kept as a constant value of 300 μm. Between the dielectric layers, there are 12 packed beads (with radius of 420 μm) regularly arranged in alternating locations inside and outside (6 beads per layer), and the spacing of adjacent beads in each layer is set as 60°.

Three typical regions are divided by the minimum and maximum distance between the center position of HV electrode and the surface of the inner beads layer (two dashed

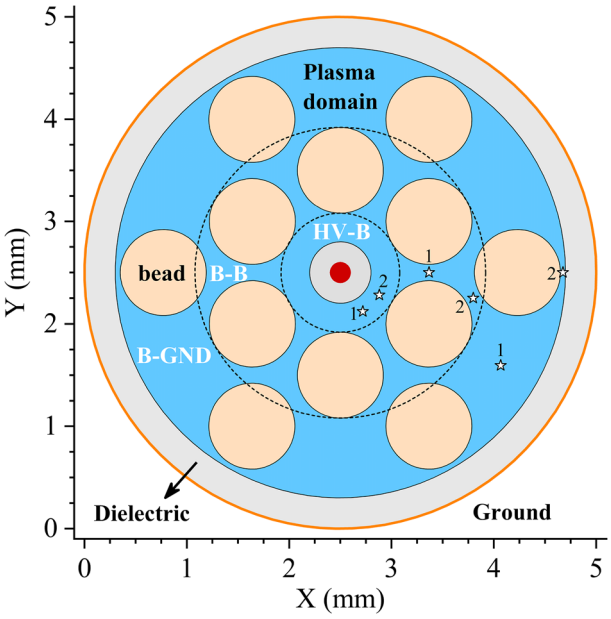

Fig. 1 Geometry of the packed bed DBD computational domain

lines in Fig. 1), namely HV to beads (HV–B), beads to beads (B–B), and beads to ground electrode (B–GND), respectively. In each region, two representative locations, at the possible path of streamer propagation, are selected to probe the evolution of electric field. For HV–B region, location 1 $L_{\mathrm{HV-B},1}$ faces the gap of bead–bead and location 2 directly faces the bead surface; for B–B and B–GND region, the midpoints of the gap between adjacent beads and between beads and dielectric layer near ground electrode are selected.

The discharge is conducted in atmospheric air at 300 K. The kinetic scheme for N_2/O_2 is taken from [47], containing 15 species and 34 reactions. As seed electrons can be created by previous pulses, especially under a high repetition rate, the initial charge density is set as 10^{15} m^{-3} and is uniformly distributed in the plasma domain based on quasi-neutrality. The applied voltage has an amplitude of 8 kV for both polarities, with a rising/falling edge of 2 ns and a duration of 6 ns. In the model, the same permittivity $\varepsilon_r = 4.2$ is used for the beads and the dielectric layers. To resolve thin surface streamers, the uniform structured mesh with a size of 3 μm is adopted in the entire domain.

Applicability of Fluid Model

With the specific PB DBD structure and the voltage amplitude used in the model, the maximal electric field in plasma domain is less than 450 kV/cm, corresponding to the reduced electric field E/N ~ 1800 Td at atmospheric pressure. As shown in Fig. 2a, good agreement for the electron energy distribution function (EEDF) calculated by Bolsig + [48], the Monte Carlo collision (MCC) program METHES [49], and our MCC module using the cross sections of air [50] is achieved, indicating that the coefficients used in the fluid model are still applicable even under this extremely condition (1800 Td). From the EEDF, it is found that the proportion of electrons with energy ε greater than 300 eV is less than ~ 10^{-7}. The mean free path of electrons can be obtained by $L_{mfp} = 1/(\sigma_{tot} N)$, where σ_{tot} is the total cross section and N is the neutral density. Taking σ_{tot} with a smallest value ~ 10^{-19} m^2 (for electrons with $\varepsilon < 0.1$ eV or $\varepsilon > 300$ eV), the upper limit of L_{mfp} is ~ 0.4 μm. Considering the smallest gap between bead and dielectric (in B–GND region) with length of $L_{gap} = 50$ μm, the Knudsen's number estimated as the ratio of L_{mpf}/L_{gap} is less than 0.008. Thus, the assumption on the continuity of fluid can be fully satisfied and the fluid model is applicable to the PB DBD structure considered in this work.

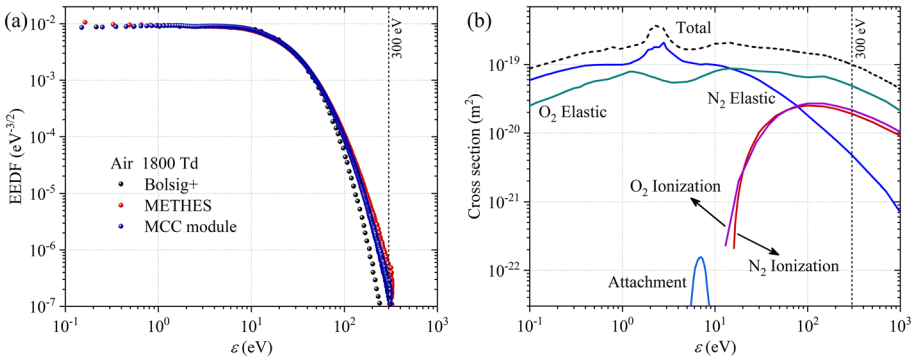

Fig. 2 **a** Electron energy distribution function (EEDF) calculated by Bolsig +, METHES, and MCC module at reduced electric field E/N = 1800 Td, and **b** cross section set of electron-air used in the model (excitation cross sections are not shown here)

Results and Discussion

The spatial distributions of energy density accumulated during the HV pulse are shown in Fig. 3. Several shared features can be found for all cases: (a) energy density mainly concentrates on the region between the inner dielectric layer and its nearest six packed beads, and gradually reduces further away from the central position; (b) peaks appear on the closest lines between the inner dielectric layer and the packed beads, while the energy density has a lower value at positions corresponding to the gap of adjacent beads; (c) since the regular arrangement of the packed beads, the energy density also presents an approximately periodic distribution (in a central angle of 60°).

Except for these similarities, the consequences caused by residual surface charges are distinct for different polarities. For the positive pulse, the coverage of energy density is obviously expanded to the entire plasma domain in the bipolar mode, while it is confined in the vicinity of the inner dielectric layer in the unipolar mode, as shown in Figs. 3b, c). Compared to the single mode, the energy is elevated both in space and along the surface of beads in the inner region in the bipolar mode, but in the periphery region, it is mainly enhanced in the gap between the packed beads.

As for the negative pulse, whether bipolar or unipolar mode, the accumulated energy density always fills the entire plasma domain and presents a relatively uniform distribution in the periphery region (Fig. 3e, f). This means that even if the residual surface charges have the same polarity of the applied HV pulse, the deposited energy can

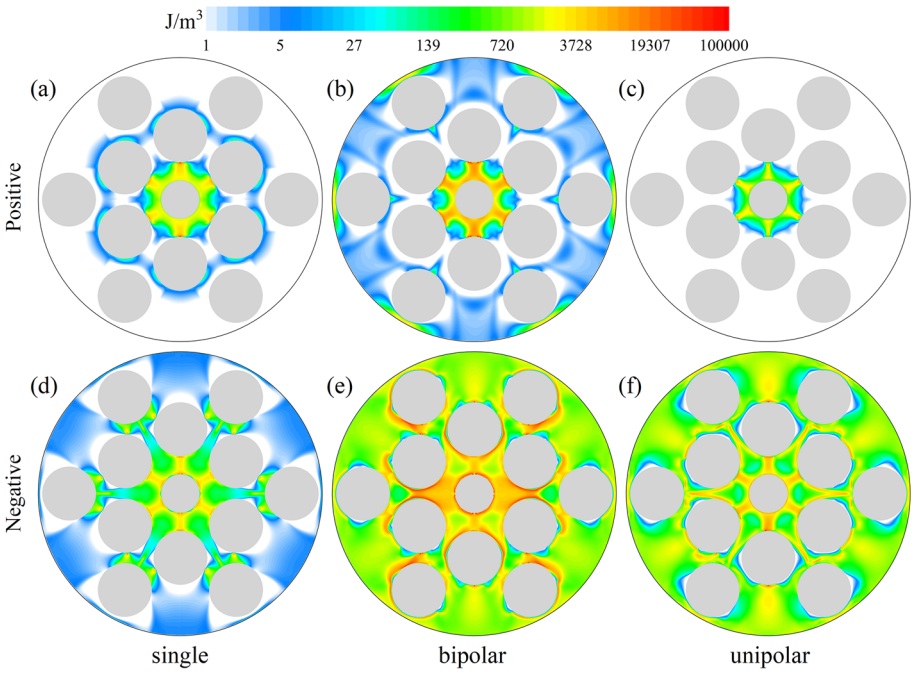

Fig. 3 Spatial distribution of the deposited energy density during the voltage pulse in single (**a** and **d**), bipolar (**b** and **e**), and unipolar (**c** and **f**) modes for positive and negative polarity

also be substantially elevated. Another characteristic is that the energy density increases remarkably along the packed beads surface.

To illustrate the importance of residual surface charges, the comparison of net charge transfer and total energy with different voltage amplitudes (6, 8, and 10 kV) and with different operating modes (single, bipolar, and unipolar) are first given in Fig. 4a–d. It is proposed that net surface charge transfer σ_{tr} is correlated with the energy coupled by the discharge pulse [51], which can be estimated as:

$$\sigma_{tr} = \int \left(\sigma_{end} - \sigma_{init}\right) dS \tag{1}$$

where σ_{init} and σ_{end} represent the amount of charges deposited at the initial and end time of discharge pulse for surface S. With increasing the voltage amplitude in single mode, a larger σ_{tr} is obtained for both polarities. As shown in Fig. 4c, for the positive pulse, the net charge transfer is remarkably enhanced in the bipolar mode because of the opposite sign between the residual surface charges and the applied pulse, while a contrary trend appears in the unipolar mode. However, for the negative pulse, due to the presence of packed beads, the net transfer of surface charges both in bipolar and unipolar modes are obviously higher.

Moreover, the total energy deposited can be obtained by calculating the product of the energy density and the volume of each cell and summing it over the plasma domain, which is found positively correlated with the net charge transfer (Fig. 4b, d). Obviously, the total energy deposited during one voltage pulse is positively correlated with the voltage amplitude. However, the total energy under a 20% increment in voltage amplitude is much less than that with an adjustment of the applied pulse sequence (bipolar mode). Noted that, even in the unipolar mode, the energy coupling is also significantly enhanced at the negative polarity, which is quite different from previous studies [46, 51].

Figure 4e, f present the relative proportion of energy density in the channel ε_{ch} and in the streamer front region ε_{fr} during the voltage rising and falling edge, divided by the intermediate instant of the pulse $t = 5$ ns. The regions where $E \leq 30$ kV/cm (breakdown threshold in air) are defined as the streamer channel. The energy ratio in channel R_{ch} is estimated as:

$$R_{ch} = \frac{\varepsilon_{ch}}{\varepsilon_{tot}} = \int \frac{P_{ch}}{P_{tot}} dt \tag{2}$$

where ε_{tot} is total energy density, P_{tot} is total power density, and P_{ch} is power density in channel. At the rising edge, although it has a diverse trend under the impact of residual surface charges, ε_{ch} is always less than half of the total power density ε_{tot}. Thus, the energy is mainly provided by the streamer front regions. At the falling edge, the presence of residual surface charges in positive polarity further reduces the proportion of ε_{ch}. For negative pulse, the trend of variation is completely opposite, that ε_{ch} greatly increases over the half of ε_{tot} and dominates in the bipolar mode.

Since the residual surface charge tremendously affects the energy deposition in different stages of discharge, it may play a critical role in plasma chemistry. For example, molecules in vibrational states can rise the energy efficiency for gas conversion and provide a more reactivity on the catalyst surface, due to the lower activation energy thresholds [52, 53]. The energy branching for each reaction is estimated as:

$$\varepsilon_{br,j} = \frac{R_j \prod_i n_i \Delta\varepsilon}{\sum_j \left(R_j \prod_i n_i \Delta\varepsilon\right)} \tag{3}$$

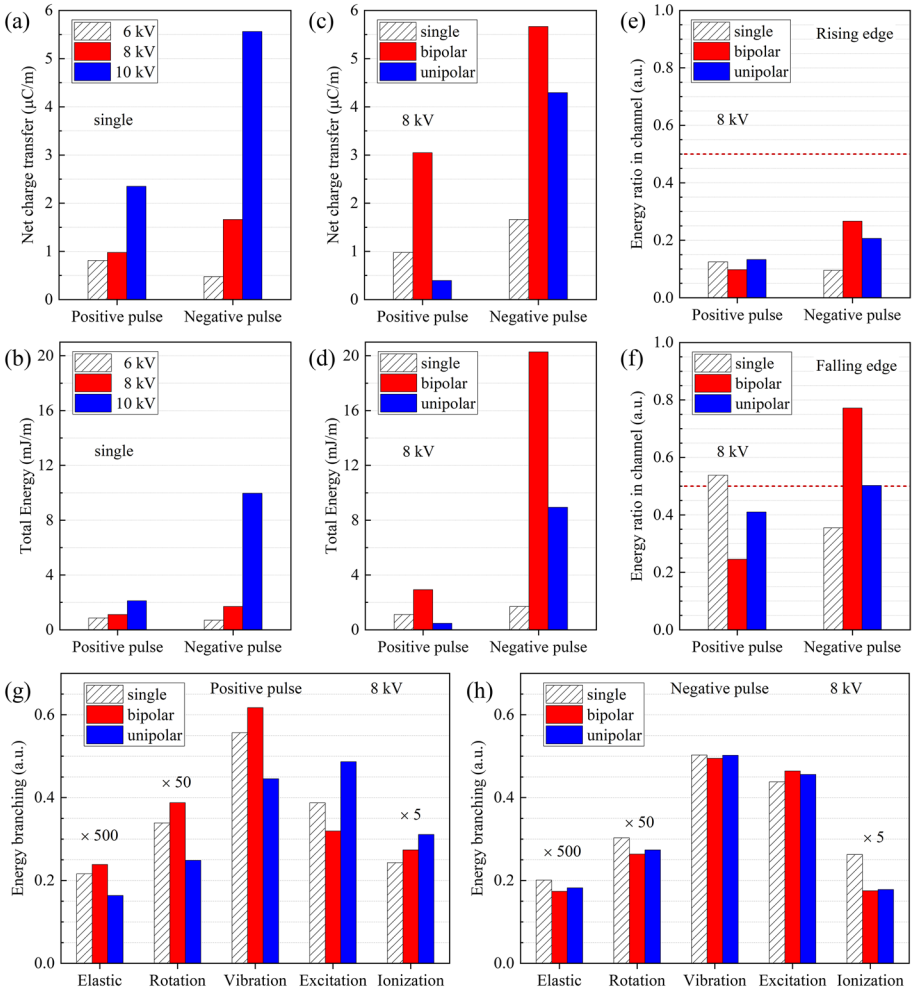

Fig. 4 Comparison of **a** and **c** net surface charge transfer, **b** and **d** total energy over the plasma domain, ratio of energy deposition in channel at **c** rising and **d** falling edge, and energy branching of **e** positive and **f** negative polarity. Conditions: **a**, **b** in single mode with different voltage amplitudes (6, 8, and 10 kV); **c**-**h** with voltage amplitude of 8 kV in different operating modes (single, bipolar, and unipolar)

where $\varepsilon_{br,j}$ is the energy branching of reaction j, R_j, n_i, and $\Delta\varepsilon$ are the corresponding rate, reactant density of species i, and enthalpy for each reaction. By summing $\varepsilon_{br,j}$ according to the reaction type, the energy branching for various processes (e.g. vibration and excitation) is obtained. Among different operating modes, the energy transferred by electrons into various processes of plasma chemistry can provide a direct insight into the alteration of the target products, as shown in Fig. 4g, h.

In both polarities, there is an agreement that a relatively large percentage of energy is spent on the vibrational and electronic excitation of molecules. But the percentage between energy branches obviously varies when operating in different modes. Specifically, for positive polarity, only the ratio of electronic excitation is reduced in the bipolar mode, while it is elevated in the unipolar mode. Combined with the amplitude of total energy over the

entire domain, the bipolar mode can provide a more evident regulation effect for energy branching.

For negative polarity, the proportion of ionization and the states with much lower threshold energies (elastic, rotational, and vibrational) is reduced in both modes, while that of electronic excitation is slightly increased. This means that residual surface charges can be affected by designing the polarity relationship between the applied pulse trains, and then adjusting the direction of discharge energy (or the target products).

Essentially, the above-mentioned characteristics of power density and energy branching are closely related to the dynamics of the local electric field, especially with the presence of residual surface charges on the packing materials. Figure 5 presents the evolution of the electric field strength at certain locations of HV–B, B–B, and B–GND regions for both polarities, aiming to reveal the impact of charge accumulation on the discharge dynamics.

For the positive pulse, when the discharge operates in the single mode, the field strength increases from zero as the applied voltage starts to rise, showing a near-Laplacian profile (Fig. 5a). The field at locations closer to the HV electrode ($L_{\mathrm{HV-B},1-2}$) first reaches the peak and then followed by a rapid decline, indicating that the breakdown occurs. After that, a second peak with a lower amplitude can be observed, but the strength at $L_{\mathrm{HV-B},2}$ is less intense, meaning a stronger self-shielding effect of plasma here. For the outer locations in the B–B and B–GND regions, the profiles of electric field are not obviously disturbed by the space charge and follow the applied voltage. Due to the enhancement in the gap between adjacent beads at different layers and beads-dielectric (near ground), field intensity at $L_{\mathrm{B-B},2}$ and $L_{\mathrm{B-GND},2}$ is higher than that at $L_{\mathrm{B-B},1}$ and $L_{\mathrm{B-GND},1}$ (lower than 30 kV/cm after the first peak).

From Fig. 5b, c, the fields have an obvious non-zero intensity at the beginning of the voltage pulse due to the presence of the residual surface charges. Similar results are also observed in [31, 32]. In the bipolar mode, a steeper decline means that the discharge starts earlier (at 0.1 ns) and the breakdown voltage drops significantly. The maximum of field is higher than 180 kV/cm, which is due to the strong accumulation of negative surface charges. The multiple-peak feature observed at $L_{\mathrm{HV-B},1}$ is accompanied by the weaker self-shielding effect (lower plasma density) compared to that of the main discharge channel. During the falling edge, the increase of field strength at $L_{\mathrm{B-B},1-2}$ and $L_{\mathrm{B-GND},1}$ indicates that the locally space charge density is low and the field is mainly provided by the surface charges, while the field first increases and then drop to almost zero at $L_{\mathrm{B-GND},2}$ due to reverse breakdown in such a small gap, both of which are consistent with Fig. 3b.

On the contrary, in the unipolar mode, the field first drops to zero and then rises again with the increase of applied voltage, indicating that the residual surface charges hinder the inception of the discharge. As shown in Fig. 5c, the breakdown instant is delayed to ~ 3.7 ns. In the falling edge, a trend similar to the single mode is found, that is, the field at $L_{\mathrm{B-B},1-2}$ and $L_{\mathrm{B-GND},1-2}$ first decreases following the voltage waveform and then increases again. This means that the discharge hardly reaches these locations and the direction of electric field provided by the applied voltage is opposite to that by surface charges. Thus, the energy density is greatly suppressed (Fig. 3c).

For the negative pulse, the situation is quite different. Axis of voltage is inverted. Compared to the positive polarity, a larger field intensity in the single mode appears at $L_{\mathrm{B-B},1}$ and $L_{\mathrm{B-GND},1-2}$ but remain a near-Laplacian behavior, indicating that no streamer or obvious space charge occurs in volume or along the dielectric surface to disturb the field distribution. But at $L_{\mathrm{B-B},2}$, the breakdown happens at ~ 4.8 ns, and the field drops to almost zero until the end of the pulse.

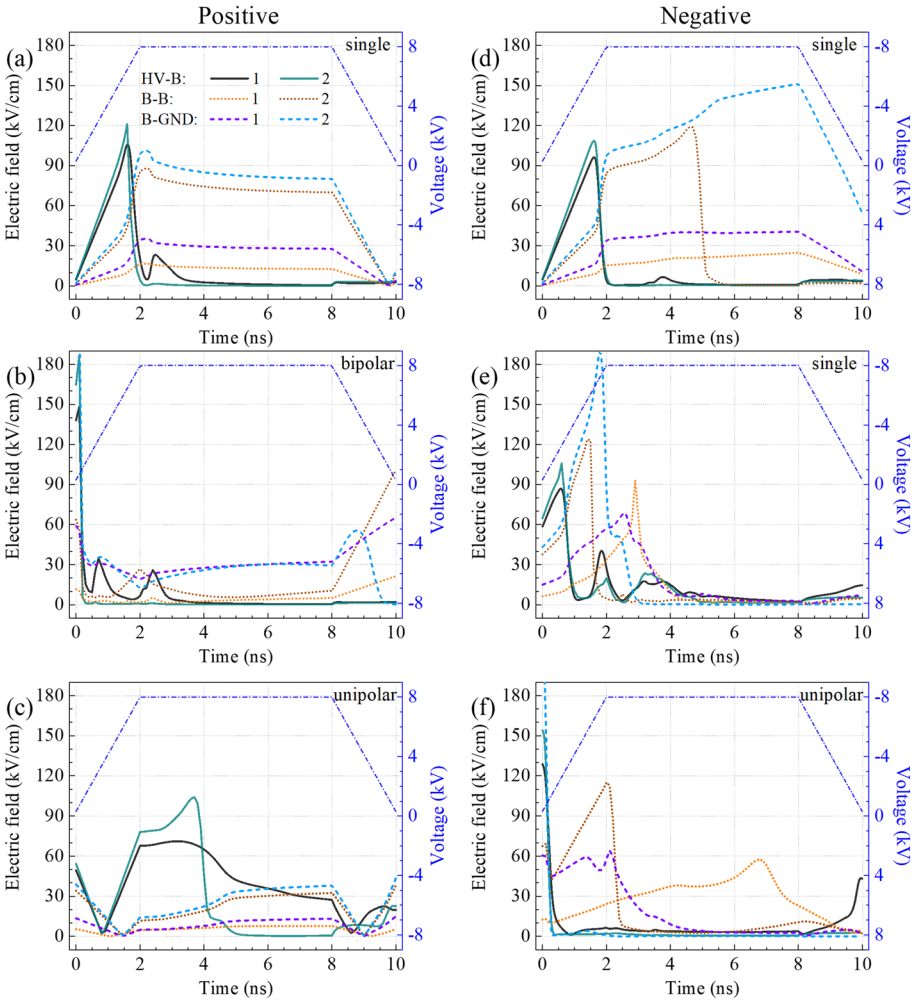

Fig. 5 Temporal evolution of electric field at certain locations in the single, bipolar, and unipolar mode for positive (left column) and negative (right column) polarity

From Fig. 5e, there is an obvious offset at the inception of voltage and the field continues to increase until breakdown happens. The field peak appears successively at different locations, indicating the propagation of the streamer. Different trends are observed in the unipolar mode. The field drops from the offset value at the voltage rising edge because of the opposite directions of electric field caused by the residual surface charges and the applied voltage. However, the maximum field in HV–B region reaching up to ~ 150 kV/cm directly leads to the breakdown near the HV electrode (Fig. 5f), rather than suppressing the discharge. This explains why the energy deposition is significantly elevated even in the unipolar mode (Fig. 3f).

Based on the above analysis, electric field at different locations varies drastically during a voltage pulse, involving the complex interaction among surface charges, beads arrangement, and streamer dynamics. Consequently, whether the discharge energy is deposited in

Fig. 6 Temporal evolution of total power density P_{tot}, power density in channel P_{ch}, and in the streamer ▶ front region P_{fr} for positive (left column) and negative (right column) polarity. Condition I: in the single, bipolar and unipolar modes with voltage amplitude of 8 kV (**a–f**); Condition II: in the single mode with different voltage amplitudes 6 kV and 10 kV (**g–j**)

the streamer front region or in the channel will influence the energy efficiency and proportion of the target products [54]. The temporal evolution of deposited power in different regions and energy branching for various reaction types are presented in Figs. 6, 7 and 8, respectively. The impact of different factors (residual surface charges and voltage amplitude) on the power deposition is also discussed.

From Figs. 6a, d, in the single mode, P_{tot} first reaches its maximum at the rising edge and then followed by a second peak with weaker intensity at the voltage plateau, corresponding to the breakdown instant at various locations (Figs. 5a, d). The first peak is accompanied by the formation of the main plasma channels (like $L_{\mathrm{HV-B},2}$), so the power density in streamer front P_{fr} dominates. For the second peak, under positive pulse, since the plasma has a weaker self-shielding effect (relatively lower density) between adjacent main plasma channels, the fluctuation of electric field leads to an increase of P_{ch} (Fig. 5a). Conversely, the second peak in negative polarity is caused by the breakdown at locations further away from the center (like $L_{\mathrm{B-B},2}$), and thus P_{fr} dominates.

For the positive pulse, the presence of residual surface charges greatly changes the behavior of the power density under different operating modes. As shown in Fig. 6b, multiple peaks of P_{tot} appear mainly at the rising edge with a maximum ~ 10^3 kW/m^3, corresponding to the fluctuations of the electric field at different locations (Fig. 5b). Then it gradually decreases during the plateau similar to the single mode. However, in the unipolar mode, P_{tot} tends to decline at the rising edge, and then reaches its maximum at the plateau with a lower amplitude (~ 10 kW/m^3), indicating a strong inhibition on the energy accumulation of discharge. At the voltage falling edge, the contribution to the power deposition between the plasma channel and the streamer front region alternately dominates.

For the negative pulse, the two-peak feature is preserved and is mainly contributed by the streamer front region in both operating modes (Fig. 6e, f). Compared to the single mode, the peak instant occurs earlier and the amplitude is larger, indicating that the power deposition during the pulse can be greatly improved regardless of the polarity of the residual surface charges. In the bipolar mode, P_{tot} is mainly provided by the plasma channel after the second peak, and this situation can continue until the end of the pulse, corresponding to the rather weak strength of electric field (Fig. 5e, f).

In order to reveal the role of residual surface charges at various regions on the energy coupling, the temporal evolution of power density in different regions ($P_{\mathrm{HV-B}}$, $P_{\mathrm{B-B}}$, and $P_{\mathrm{B-GND}}$) are presented in Fig. 7. For the cases without pre-pulse (single mode), $P_{\mathrm{HV-B}}$ first reaches the maximum at the voltage rising edge for both polarities (Fig. 7a, d), and then distinctions among different regions appear. For the positive pulse, $P_{\mathrm{HV-B}}$ provides most of the contribution during the whole discharge, while $P_{\mathrm{B-B}}$ in negative pulse starts to become dominant after the peak of $P_{\mathrm{HV-B}}$. As discharges operated in bipolar/unipolar modes, the location and amount of residual surface charges alter the temporal behavior of power deposition.

For the positive pulse, residual surface charges in the bipolar mode can cover the entire discharge domain, leading to an earlier peak instant of power density for all regions. The amplitude of $P_{\mathrm{B-B}}$ and $P_{\mathrm{B-GND}}$ is elevated to almost the same order of magnitude as that of $P_{\mathrm{HV-B}}$, and alternately dominates (Fig. 7b). In the unipolar mode, because residual charges

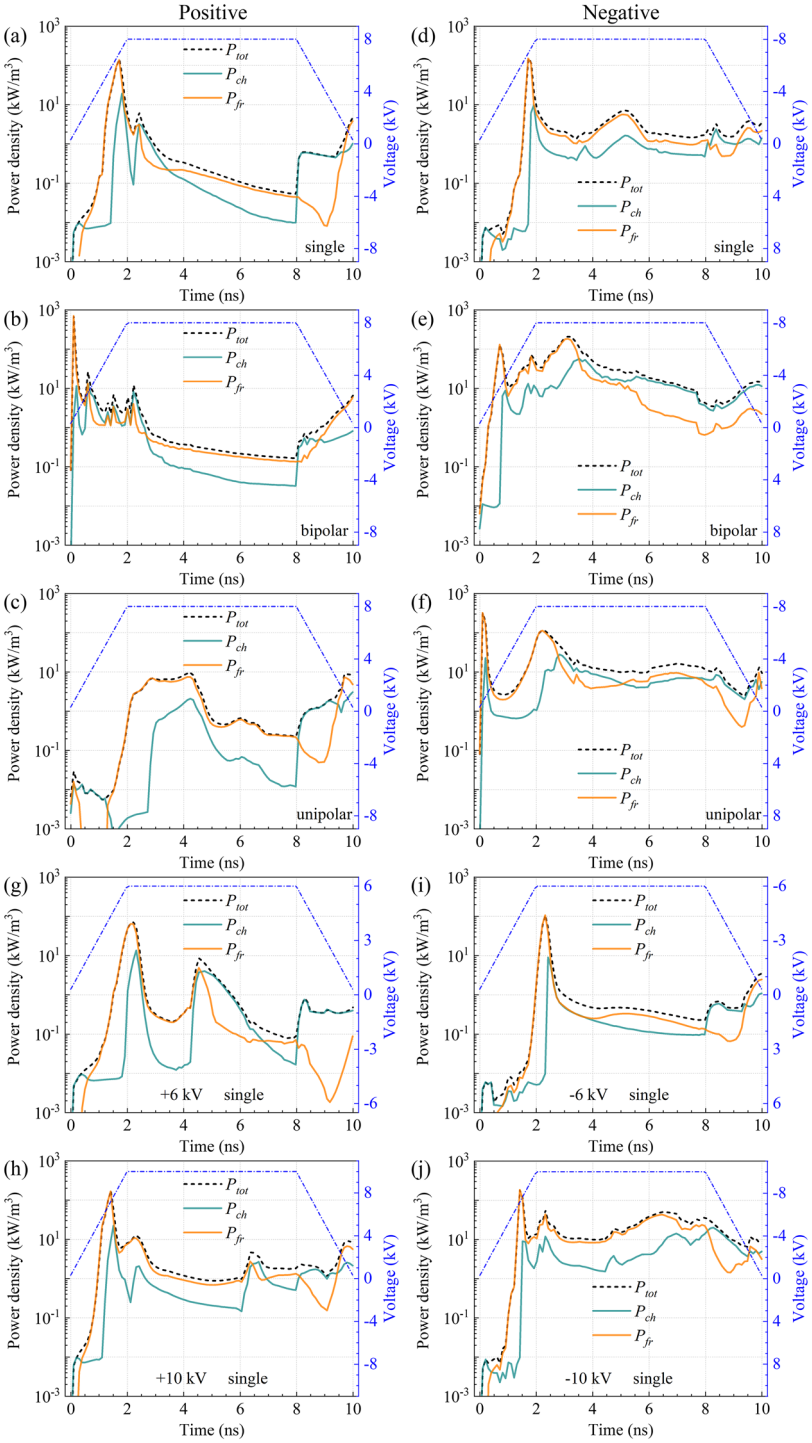
Positive
Negative
(a)
(b)
(c)
(d)
(e)
(f)
(g)
(h)
(i)
(j)
P_{tot}
P_{ch}
P_{fr}
Power density (kW/m^3)
Voltage (kV)
Time (ns)
single
bipolar
unipolar
+6 kV single
-6 kV single
+10 kV single
-10 kV single

Fig. 7 Temporal evolution of total power density P_{tot}, power density in the HV–Beads, Beads–Beads, and Beads–Ground region for positive (left column) and negative (right column) polarity. Condition I: in the single, bipolar and unipolar modes with voltage amplitude of 8 kV (**a**–**f**); Condition II: in the single mode with different voltage amplitude 6 kV and 10 kV (**g**–**j**)

are mainly deposited on the beads surface facing the HV electrode, the charges having the same polarity with the applied voltage further restrict the discharge within the gap between HV and inner beads layer. Thus, $P_{\mathrm{B–B}}$ and $P_{\mathrm{B–GND}}$ are significantly inhibited (Fig. 7c).

For the negative pulse, $P_{\mathrm{HV–B}}$ in bipolar mode has a lower peak than that in the single mode due to the reduction of breakdown voltage (Fig. 7e). Then, both $P_{\mathrm{B–B}}$ and $P_{\mathrm{B–GND}}$ significantly increase and remain higher than $P_{\mathrm{HV–B}}$ during voltage plateau. Combined with Fig. 3e, it is found that residual charges enhance the discharge intensity along the beads surface and improve the plasma uniformity in the B–GND region. Conversely, in unipolar mode, a large amount of residual surface charges directly causes the breakdown, enhancing the power deposition in all regions at the voltage inception (Fig. 7f).

To distinguish the effects of residual surface charges and applied voltage amplitude on the energy coupling, the temporal evolution of power density is given, based on the breakdown threshold (Fig. 6g–j) and space region (Fig. 7g–j). With increasing the voltage amplitude from 6 to 10 kV, both P_{fr} and P_{ch} are elevated as expected, but a larger increment appears for P_{fr} (especially for the first peak at the rising edge). Moreover, from Fig. 7, it can be found that the increment in P_{tot} are mainly provided by that deposited at B–B and B–GND regions. However, compared to the effect caused by residual surface charges (e.g. bipolar mode), the increase in P_{tot} are still weaker. This further indicates that the regulation of residual surface charges is more effective than directly increasing voltage amplitude to achieve the same effect on enhancing energy deposition.

As for the energy branching, its temporal behavior presents several distinct features depending on the threshold of reactions. In the single mode (Figs. 8a, d), reactions with lower energy thresholds, such as elastic, rotational and vibrational, have their peak value at the initial instant of HV pulse. Consequently, the corresponding ratios first decrease due to the rise of applied voltage and then gradually recover to the previous higher level, which remains until the falling edge of the pulse. On the contrary, excitation and ionization reactions with relatively higher energy thresholds show the opposite tendency.

For positive polarity, the energy ratio of the excitation and ionization reactions at the initial discharge instant first increases and then decreases at the voltage rising edge, while that of reactions with lower energy threshold is elevated. After entering the voltage plateau period, the energy branching in vibrational reaction always dominates in bipolar mode, whereas the maximum amplitude between the vibrational and excitation states varies alternately in unipolar mode (Fig. 8b, c). Residual surface charges present a completely distinct effect on the energy branching for the two operating modes, especially between vibration and excitation states (Fig. 3e).

As can be seen from Fig. 8e, f, the energy ratio of excitation and ionization reactions in the bipolar mode increases at the voltage rising edge, while in the unipolar mode, although that of these two reaction types is enhanced at the initial instant of the pulse, it tends to decrease as the voltage increases. However, in the remaining discharge stage, the temporal behavior of different reaction types is similar between the two operating modes. As a result, for negative polarity, the alteration of residual surface charges on the energy branching tends to be approximately consistent, rather than presents the reverse effect as in the positive pulse.

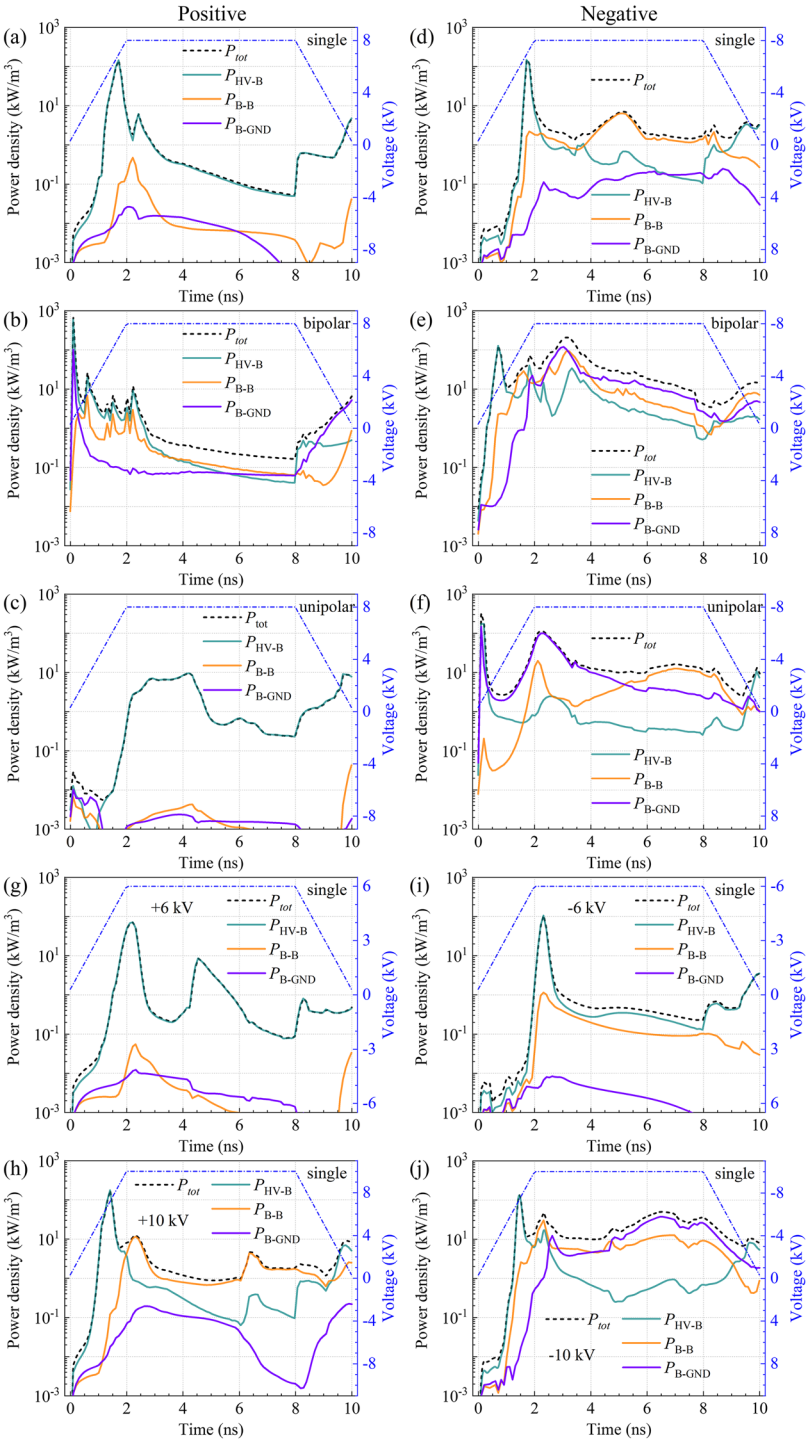
Positive
Negative
(a)
single
(b)
bipolar
(c)
unipolar
(d)
single
(e)
bipolar
(f)
unipolar
(g)
single
+6 kV
(h)
single
+10 kV
(i)
single
-6 kV
(j)
single
-10 kV
P_{tot}
P_{HV-B}
P_{B-B}
P_{B-GND}
Power density (kW/m^3)
Voltage (kV)
Time (ns)

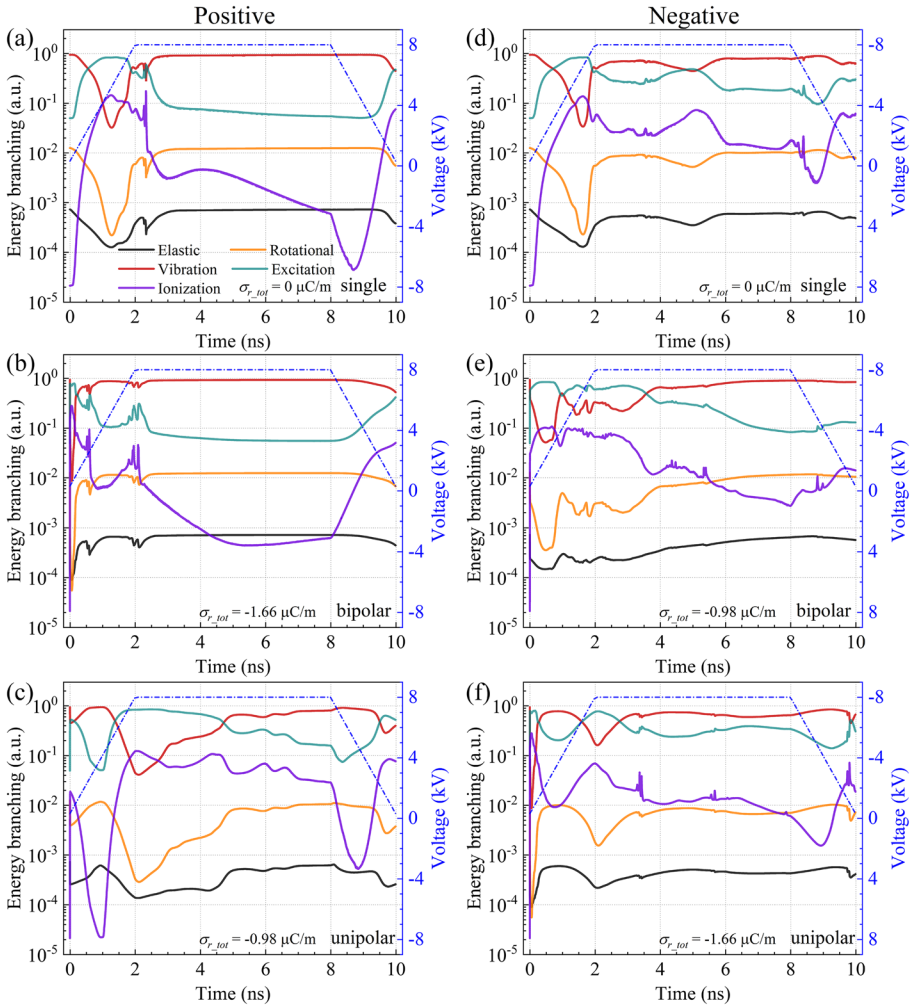

Fig. 8 Temporal evolution of energy branching for various reaction types in the single, bipolar, and unipolar modes for positive (left column) and negative (right column) polarity. σ_{r_tot} is the total amount of residual surface charges

The obtained results demonstrate that, in the PB DBD reactors, residual surface charges can greatly alter the energy deposition process and its branching by affecting the distribution of electric fields, which is a feasible approach to regulate the target products in a macroscopic view. However, limited by the computational burden, such complex spatial arrangement of packed beads and the intrinsic three-dimensional streamer-dielectric interactions (e.g. branching behavior) cannot be taken into account in the 2D fluid model, which has beyond the scope of this work. For further investigation, it is necessary to consider the more realistic layout of PB DBD and the stochastic nature of streamers with a kinetic treatment for electrons.

Conclusion

In this work, the discharge dynamics and energy coupling in a coaxial packed-bed DBD reactor are investigated by a 2D fluid model, taking into account the residual surface charges on the surface of dielectric and packing beads. Temporal evolutions of the electric field, instantaneous power density, and energy branching for discharges operated in the single, bipolar, and unipolar modes in both polarities are presented.

With positive polarity, the accumulated energy during a discharge pulse is obviously elevated in the bipolar mode, whereas it is suppressed and confined within the inner domain in the unipolar mode. Conversely, a larger net charge transfer significantly enhances the energy deposition process in the negative polarity, regardless of the operating modes. Moreover, the presence of residual surface charges alters the proportions of power density in the plasma channel and the streamer front region, as well as the percentage of energy consumption among different electron collision processes, showing a regulation effect on the characteristics of plasma chemistry.

The energy coupling properties are strongly correlated with the dynamics of the electric field. With the presence of residual surface charges, the electric field shows a significant nonzero offset at the beginning of the voltage pulse. In the bipolar mode, the field is enhanced by the accumulated charges in the direction of the applied voltage, leading to a sharp drop in the breakdown voltage and an earlier inception of the discharge. In the unipolar mode, opposite effects are observed in the positive polarity, while a strong field enhancement induced by the intense residual surface charges directly leads to the breakdown in the negative polarity, and thus no suppressing effect occurs.

The simulated results demonstrate the critical role of residual surface charge in the regulation of discharge dynamics, power deposition, and energy branching, providing an insight into the relationship between plasma behavior and energy coupling in the packed-bed DBD reactor.

Appendix: Basic Equations and Boundary Conditions

The temporal evolution of species is solved by the drift–diffusion-reaction equations,

$$\frac{\partial n_i}{\partial t} + \nabla \cdot \boldsymbol{\Gamma}_i = S_i + S_{ph},\ i = 1, 2, \ldots, N_{total} \tag{4}$$

$$\boldsymbol{\Gamma}_i = -D_i \nabla n_i - \left(\frac{q_i}{|q_i|}\right)\mu_i n_i \nabla \phi,\ i = 1, 2, \ldots, N_{charge} \tag{5}$$

$$\frac{\partial\left(n_\epsilon \epsilon_m\right)}{\partial t} + \nabla \cdot \boldsymbol{\Gamma}_\epsilon = -\left|q_e\right| \cdot E \cdot \boldsymbol{\Gamma}_\epsilon - P\left(\epsilon_m\right) \tag{6}$$

$$\boldsymbol{\Gamma}_\epsilon = -D_\epsilon \nabla\left(n_\epsilon \epsilon_m\right) - n_\epsilon \epsilon_m \mu_\epsilon E \tag{7}$$

where n_i, q_i, D_i and μ_i are density, charge, diffusion coefficient and mobility of species i. $\boldsymbol{\Gamma}$ is the flux term, and its drift part is limited by the UNO3 scheme [55]. S and S_{ph} are the source terms for gas-phase reaction and photoionization. To calculate S_{ph}, the three-term Helmholtz equations are solved in air, for which the fitting parameters are taken from [56]. The electron energy conservation equation is coupled to resolve the plasma-dielectric

interaction. $\boldsymbol{E}$ is the electric field. $P(\epsilon_m)$ represents the collision power lost for electrons and is obtained by Bolsig + [48]. The model is closed by the Poisson equation with consideration of both the charge density in space ρ and on the dielectric surface σ,

$$\nabla\left(\varepsilon_0\varepsilon_r\nabla\phi\right) = -\rho - \sigma \tag{8}$$

$$\frac{\partial\sigma}{\partial t} = \sum_i q_i\left(-\nabla\cdot\boldsymbol{\Gamma}_i\right) \tag{9}$$

Specific boundary conditions applied in the model are given below. For drift–diffusion-reaction equations, simplified boundary conditions at metal and dielectric surfaces are taken into account [57, 58]. A zero-flux boundary condition is imposed at plasma-surface interfaces for neutral species. As for charged species, different boundary conditions are considered based on the drift direction toward the surface.

$$\boldsymbol{\Gamma}_e\cdot n_s = (a-1)\mu_e n_e E\cdot n_s - a\sum\gamma\boldsymbol{\Gamma}_{i,+}\cdot n_s \tag{10}$$

$$\boldsymbol{\Gamma}_\epsilon\cdot n_s = (a-1)\left(\frac{5}{2}k_bT_e\right)\mu_e n_e E\cdot n_s - a\left(\frac{5}{2}k_bT_{se}\right)\sum\gamma\boldsymbol{\Gamma}_{i,+}\cdot n_s \tag{11}$$

$$\boldsymbol{\Gamma}_{i,-}\cdot n_s = (a-1)\mu_{i,-}n_{i,-}E\cdot n_s \tag{12}$$

$$\boldsymbol{\Gamma}_{i,+}\cdot n_s = a\mu_{i,+}n_{i,+}E\cdot n_s \tag{13}$$

where Γ_e, Γ_ϵ, $\Gamma_{i,-}$, $\Gamma_{i,+}$ are electron, electron energy, negative ion, and positive ion fluxes at the boundary, respectively. n_s is the normal vector pointing outward. For $\boldsymbol{E}\cdot n_s < 0$, $a = 1$; otherwise $a = 0$. γ (taken as 0.1) is the secondary emission coefficient by impact of ions. T_e and T_{se} are the temperature of electron in bulk and secondary electron emitted from surface. T_{se} is assumed as 1 eV [59].

For Poisson equation, Neumann condition is assumed at open boundaries of computational domain, and Dirichlet condition is applied for metal surfaces with specific voltages. As for the dielectric regions, the surface charge accumulation is calculated during each time step by collecting the flux term of charged species flowing towards the dielectric (Eq. 9), and then is stored as additional source when solving Poisson equation.

For various coordinate systems, the direction of normal vector at the surface is the key of boundary condition processing. For example, the expression of flux term at boundaries in polar coordinate (r, θ) can be obtained by combining the components along the x and y direction in Cartesian coordinate:

$$\vec{r} = \cos\theta\vec{x} + \sin\theta\vec{y} \tag{14}$$

$$\vec{\theta} = -\sin\theta\vec{x} + \cos\theta\vec{y} \tag{15}$$

where $\vec{r}$, $\vec{\theta}$, $\vec{x}$, $\vec{y}$ are the base vectors in the polar and Cartesian coordinate, respectively. The descriptions on the physical process by these two coordinate systems are essentially equivalent. Thus, although the PB DBD structure is in cylindrical symmetry, it is appropriate to analyze the discharge dynamics using 2D Cartesian coordinate.

Acknowledgements This work was supported by the National Science Fund for Distinguished Young Scholars (Grant No. 51925703), the National Natural Science Foundation of China (Grant Nos. 52022096,

52277167), the Young Elite Scientist Sponsorship Program by CAST (Grant No. YESS20210402). The authors are thankful to Dr Yifei Zhu for fruitful discussions.

Author Contributions CR and BH performed the investigation, data analysis, wrote the main manuscript text and prepared the Figs. 1, 2, 3, 4, 5, 6, 7 and 8; YL and CZ participated the investigation and validation; TS performed result analysis and discussion. All authors reviewed the manuscript.

Funding Tao Shao: National Science Fund for Distinguished Young Scholars (Grant No. 51925703), Cheng Zhang: National Natural Science Foundation of China (Grant No. 52022096), Bangdou Huang: National Natural Science Foundation of China (Grant No. 52277167), Young Elite Scientist Sponsorship Program by CAST (Grant No. YESS20210402).

Data Availability The authors confirm that the data supporting the findings of this study are available within the manuscript.

Declarations

Conflict of interest The authors declare no competing financial interest or personal nature.

References

1. Neyts E, Ostrikov K, Sunkara M, Bogaerts A (2015) Plasma catalysis: synergistic effects at the nanoscale. Chem Rev 115:13408–13446. https://doi.org/10.1021/acs.chemrev.5b00362
2. Xu S, Chansai S, Stere C, Inceesungvorn B, Goguet A, Wangkawong K, Rebecca S, Al-Janabi N, Hardacre C, Martin P, Fan X (2019) Sustaining metal-organic frameworks for water-gas shift catalysis by non-thermal plasma. Nat Catal 2:142–148. https://doi.org/10.1038/s41929-018-0206-2
3. Chawdhury P, Wang Y, Ray D, Mathieu S, Wang N, Harding J, Bin F, Tu X, Subrahmanyam C (2021) A promising plasma-catalytic approach towards single-step methane conversion to oxygenates at room temperature. Appl Catal B 284:119735. https://doi.org/10.1016/j.apcatb.2020.119735
4. Bogaerts A, Neyts E, Guaitella O, Murphy A (2022) Foundations of plasma catalysis for environmental applications. Plasma Sources Sci Technol 31:053002. https://doi.org/10.1088/1361-6595/ac5f8e
5. Liu L, Zhang Z, Das S, Xi S, Kawi S (2020) $LaNiO_3$ as a precursor of Ni/La_2O_3 for reverse water-gas shift in DBD plasma: effect of calculation temperature. Energy Convers Manag 206:112475. https://doi.org/10.1016/j.enconman.2020.112475
6. Dou L, Liu Y, Gao Y, Li J, Hu X, Zhang S, Ostrikov K, Shao T (2022) Disentangling metallic cobalt sites and oxygen vacancy effects in synergistic plasma-catalytic CO_2/CH_4 conversion into oxygenates. Appl Catal B 318:121830. https://doi.org/10.1016/j.apcatb.2022.121830
7. Mei D, Sun M, Liu S, Zhang P, Fang Z, Tu X (2023) Plasma-enabled catalytic dry reforming of CH_4 into syngas, hydrocarbons and oxygenates: insight into the active metals of γ-Al_2O_3 supported catalysts. J CO_2 Util 67:102307. https://doi.org/10.1016/j.jcou.2022.102307
8. Hong J, Prawer S, Murphy A (2018) Plasma catalysis as an alternative route for ammonia production: status, mechanisms, and prospects for progress. ACS Sustainable Chem Eng 6:115–131. https://doi.org/10.1021/acssuschemeng.7b02381
9. Mehta P, Barboun P, Herrera F, Kim J, Rumbach P, Go D, Hicks J, Schneider W (2018) Overcoming ammonia synthesis scaling relations with plasma-enabled catalysis. Nat Catal 1:269–275. https://doi.org/10.1038/s41929-018-0045-1
10. Ma Y, Wang Y, Harding J, Tu X (2021) Plasma-enhanced N_2 fixation in a dielectric barrier discharge reactor: effect of packing materials. Plasma Sources Sci Technol 30:105002. https://doi.org/10.1088/1361-6595/ac2412
11. Kogelschatz U (2003) Dielectric-barrier discharges: their history, discharge physics, and industrial applications. Plasma Chem Plasma Process 23:1–46. https://doi.org/10.1023/A:1022470901385
12. Veerapandian S, Geyter N, Giraudon J, Morin J, Tabaei P, Weireld G, Laemont A, Leus K, Voort P, Lamonier J, Morent R (2022) Effect of non-thermal plasma in the activation and regeneration of 13X zeolite for enhanced VOC elimination by cycled storage and discharge process. J Clean Prod 364:132687. https://doi.org/10.1016/j.jclepro.2022.132687

13. Michielsen I, Uytdenhouwen Y, Pype J, Michielsen B, Mertens J, Reniers F, Meynen V, Bogaerts A (2017) CO_2 dissociation in a packed bed DBD reactor: first steps towards a better understanding of plasma catalysis. Chem Eng J 326:477–488. https://doi.org/10.1016/j.cej.2017.05.177
14. Cui Z, Zhou C, Jafarzadeh A, Zhang X, Hao Y, Li L, Bogaerts A (2023) SF_6 degradation in a γ-Al_2O_3 packed DBD system: effects of hydration, reactive gases and plasma-induced surface charges. Plasma Chem Plasma Process 43:635–656. https://doi.org/10.1007/s11090-023-10320-3
15. Zeng X, Zhang S, Liu Y, Hu X, Ostrikov K, Shao T (2023) Energy-efficient pathways for pulsed-plasma-activated sustainable ammonia synthesis. ACS Sustainable Chem Eng 11:1110–1120. https://doi.org/10.1021/acssuschemeng.2c06259
16. Snoeckx R, Heijkers S, Van Wesenbeeck K, Lenaerts S, Bogaerts A (2016) CO_2 conversion in a dielectric barrier discharge plasma: N_2 in the mix as a helping hand or problematic impurity? Energy Environ Sci 9:999–1011. https://doi.org/10.1039/C5EE03304G
17. Bogaerts A, Berthelot A, Heijkers S, Kolev S, Snoeckx R, Sun S, Trenchev G, Van Laer K, Wang W (2017) CO_2 conversion by plasma technology: insights from modeling the plasma chemistry and plasma reactor design. Plasma Sources Sci Technol 26:063001. https://doi.org/10.1088/1361-6595/aa6ada
18. Mei D, Zhang P, Duan G, Liu S, Zhou Y, Fang Z, Tu X (2022) CH_4 reforming with CO_2 using a nanosecond pulsed dielectric barrier discharge plasma. J CO_2 Util 62:102073. https://doi.org/10.1016/j.jcou.2022.102073
19. Zhang S, Gao Y, Sun H, Fan Z, Shao T (2021) Dry reforming of methane by microsecond pulsed dielectric barrier discharge plasma: optimizing the reactor structures. High Volt 7:718–729. https://doi.org/10.1049/hve2.12201
20. Whitehead J (2016) Plasma-catalysis: the known knowns, the known unknowns and the unknown unknowns. J Phys D Appl Phys 49:243001. https://doi.org/10.1088/0022-3727/49/24/243001
21. Bogaerts A, Tu X, Whitehead J, Genti G, Lefferts L, Guaitella O, Azzolina-Jury F, Kim H, Murphy A, Schneider W, Nozaki T, Hicks J, Rousseau A, Thevenet F, Khacef A, Carreon M (2020) The 2020 plasma catalysis roadmap. J Phys D Appl Phys 53:443001. https://doi.org/10.1088/1361-6463/ab9048
22. Kim H, Teramoto Y, Ogata A, Takagi H, Nanba T (2016) Plasma catalysis for environmental treatment and energy applications. Plasma Chem Plasma Process 36:45–72. https://doi.org/10.1007/s11090-015-9652-7
23. Brandenburg R (2017) Dielectric barrier discharges: progress on plasma sources and on the understanding of regimes and single filaments. Plasma Sources Sci. Technol 26:053001. https://doi.org/10.1088/1361-6595/aa6426
24. Li R, Tang Q, Yin S, Sato T (2007) Investigation of dielectric barrier discharge dependence on permittivity of barrier materials. Appl Phys Lett 90:131502. https://doi.org/10.1063/1.2716848
25. Uytdenhouwen Y, Bal K, Michielsen I, Neyts E, Meynen V, Cool P, Bogaerts A (2019) How process parameters and packing material tune chemical equilibrium and kinetics in plasma-based CO_2 conversion. Chem Eng J 372:1253–1264. https://doi.org/10.1016/j.cej.2019.05.008
26. Liu S, Winter L, Chen J (2020) Review of plasma-assisted catalysis for selective generation of oxygenates from CO_2 and CH_4. ACS Catal 10:2855–2871. https://doi.org/10.1021/acscatal.9b04811
27. Zhao Z, Li J (2020) Repetitively pulsed gas discharges: memory effect and discharge mode transition. High Volt 5:569–582. https://doi.org/10.1049/hve.2019.0383
28. Zhang B, Zhang G (2017) Interpretation of the surface charge decay kinetics on insulators with different neutralization mechanisms. J Appl Phys 121:105105. https://doi.org/10.1063/1.4978001
29. Stollenwerk L, Laven J, Purwins H (2007) Spatially resolved surface-charge measurement in a planar dielectric-barrier discharge system. Phys Rev Lett 98:255001. https://doi.org/10.1103/PhysRevLett.98.255001
30. Li T, Yan H, Li J, Schulze J, Yu S, Song J, Zhang Q (2022) The role of surface charge and its decay in surface dielectric barrier discharges. Plasma Sources Sci Technol 31:055016. https://doi.org/10.1088/1361-6595/ac676e
31. Simeni M, Tang Y, Frederickson K, Adamovich I (2018) Electric field distribution in a surface plasma flow actuator powered by ns discharge pulse trains. Plasma Sources Sci Technol 27:104001. https://doi.org/10.1088/1361-6595/aae1c8
32. Huang B, Zhang C, Adamovich I, Akishev Y, Shao T (2020) Surface ionization wave propagation in the nanosecond pulsed surface dielectric barrier discharge: the influence of dielectric material and pulse repetition rate. Plasma Sources Sci Technol 29:044001. https://doi.org/10.1088/1361-6595/ab7854
33. Van Laer K, Bogaerts A (2016) Influence of gap size and dielectric constant of the packing material on the plasma behavior in a packed bed DBD reactor: a fluid modelling study. Plasma Process Polym 14:1600129. https://doi.org/10.1002/ppap.201600129

34. Van Laer K, Bogaerts A (2017) How bead size and dielectric constant affect the plasma behaviour in a packed bed plasma reactor: a modelling study. Plasma Sources Sci Technol 26:085007. https://doi.org/10.1088/1361-6595/aa7c59
35. Zhao P, Gu J, Wang H, Zhang Y, Xu X, Jiang W (2020) How bead shapes affect the plasma streamer characteristics in packed-bed dielectric barrier discharges: a kinetic modeling study. Plasma Sci Technol 22:034013. https://doi.org/10.1088/2058-6272/ab65b3
36. Wang W, Butterworth T, Bogaerts A (2021) Plasma propagation in a single bead DBD reactor at different dielectric constants: insights from fluid modelling. J Phys D Appl Phys 54:214004. https://doi.org/10.1088/1361-6463/abe8ff
37. Kang W, Kim H, Teramoto Y, Ogata A, Lee J, Kim D, Min H, Song Y (2018) Surface streamer propagation on an alumina bead: experimental observation and numerical modeling. Plasma Sources Sci Technol 27:015018. https://doi.org/10.1088/1361-6595/aaa7d0
38. Engeling K, Kruszelnicki J, Kushner M, Foster J (2018) Time-resolved evolution of micro-discharges, surface ionization waves and plasma propagation in a two-dimensional packed bed reactor. Plasma Sources Sci Technol 27:085002. https://doi.org/10.1088/1361-6595/aad2c5
39. Xiong R, Zhao P, Wang H, Zhang Y, Jiang W (2020) Impact of different packing beads methods for streamer generation and propagation in packed-bed dielectric barrier discharge. J Phys D Appl Phys 53:185202. https://doi.org/10.1088/1361-6463/ab6ccf
40. Mujahid Z, Korolov I, Liu Y, Mussenbrock T, Schulze J (2022) Propagation dynamics and interaction of multiple streamers at and above adjacent dielectric pellets in a packed bed plasma reactor. J Phys D Appl Phys 55:495201. https://doi.org/10.1088/1361-6463/ac99ea
41. Cheng H, Ma M, Zhang Y, Liu D, Lu X (2020) The plasma enhanced surface reactions in a packed bed dielectric barrier discharge reactor. J Phys D Appl Phys 53:144001. https://doi.org/10.1088/1361-6463/ab651e
42. Kruszelnicki J, Engeling K, Foster J, Kushner M (2021) Interactions between atmospheric pressure plasmas and metallic catalyst particles in packed bed reactors. J Phys D Appl Phys 54:104001. https://doi.org/10.1088/1361-6463/abcc92
43. Zhu Y, Chen X, Wu Y, and Starikovskaia S M (2021) PASSKEy code[software]. http://www.plasma-tech.net/parser/passkey/ (Science and Technology of Plasma Dynamics Laboratory, Xi'an, China and Laboratoire de Physique des Plasmas, Paris, France).
44. Zhu Y, Chen X, Wu Y, Hao J, Ma X, Lu P, Tardiveau P (2021) Simulation of ionization-wave discharges: a direct comparison between the fluid model and E-FISH measurements. Plasma Sources Sci Technol 30:075025. https://doi.org/10.1088/1361-6595/ac0714
45. Ren C, Huang B, Qiu J, Zhang C, Qi B, Chen W, Shao T (2022) Is an extended barrier-free discharge under nanosecond-pulse excitation really diffuse? J Phys D Appl Phys 55:235204. https://doi.org/10.1088/1361-6463/ac4f0d
46. Ren C, Huang B, Zhang C, Qi B, Chen W, Shao T (2023) Impact of surface charges on energy deposition in surface dielectric barrier discharge: a modeling investigation. Plasma Sources Sci Technol 32:025004. https://doi.org/10.1088/1361-6595/acb4b9
47. Zhu Y, Starikovskaia S (2018) Fast gas heating of nanosecond pulsed surface dielectric barrier discharge: spatial distribution and fractional contribution from kinetics. Plasma Sources Sci. Technol. 27:124007. https://doi.org/10.1088/1361-6595/aaf40d
48. Hagelaar G, Pitchford L (2005) Solving the Boltzmann equation to obtain electron transport coefficients and rate coefficients for fluid models. Plasma Sources Sci Technol 14:722–733. https://doi.org/10.1088/0963-0252/14/4/011
49. Rabie M, Franck CM (2016) METHES: a Monte Carlo collision code for the simulation of electron transport in low temperature plasmas. Comput Phys Commun 203:268. https://doi.org/10.1016/j.cpc.2016.02.022
50. SIGLO database, Phelps database, www.lxcat.net. Accessed 13 Mar 2021
51. Leonov S, Petrishchev V, Adamovich I (2014) Dynamics of energy coupling and thermalization in barrier discharges over dielectric and weakly conducting surfaces on μs to ms time scales. J Phys D Appl Phys 47:465201. https://doi.org/10.1088/0022-3727/47/46/465201
52. Snoeckx R, Bogaerts A (2016) Plasma technology—a novel solution for CO_2 conversion? Chem Soc Rev 46:5805. https://doi.org/10.1039/c6cs00066e
53. Mehta P, Barboun P, Go D, Hicks J, Schneider W (2019) Catalysis enable by plasma activation of strong chemical bonds: a review. ACS Energy Lett 4:1115. https://doi.org/10.1021/acsenergylett.9b00263
54. Guo B, Teunissen J (2023) A computational study on the energy efficiency of species production by single-pulse streamers in air. Plasma Sources Sci. Technol 32:025001. https://doi.org/10.1088/1361-6595/acb462

55. Li J (2008) Upstream nonoscillatory advection schemes. Mon Weather Rev 136:4709. https://doi.org/10.1175/2008MWR2451.1
56. Bourdon A, Pasko V, Liu N, Celestin S, Segur P, Marode E (2007) Efficient models for photoionization produced by non-thermal gas discharges in air based on radiative transfer and the Helmholtz equations. Plasma Sources Sci Technol 16:656–678. https://doi.org/10.1088/0963-0252/16/3/026
57. Pechereau F, Jansky J, Bourdon A (2012) Simulation of the reignition of a discharge behind a dielectric layer in air at atmospheric pressure. Plasma Sources Sci Technol 21:055011. https://doi.org/10.1088/0963-0252/21/5/055011
58. Zhang P, Kortshagen U (2006) Two-dimensional numerical study of atmospheric pressure glows in helium with impurities. J Phys D Appl Phys 39:153–163. https://doi.org/10.1088/0022-3727/39/1/023
59. Nagaraja S, Yang V, Adamovich I (2013) Multi-scale modeling of pulsed nanosecond dielectric barrier plasma discharges in plane-to-plane geometry. J Phys D Appl Phys 46:155205. https://doi.org/10.1088/0022-3727/46/15/155205